ACS Energy Letters

http://pubs.acs.org/journal/aelccp

LETTER

Dielectric−Metallic Double-Gradient Composition Design for Stable Zn Metal Anodes

Jin-Lin Yang,[#] Lingli Liu,[#] Zehua Yu, Pengbo Chen, Jia Li, Putu Andhita Dananjaya, Eng Kang Koh, Wen Siang Lew, Kang Liu, Peihua Yang,* and Hong Jin Fan*

Cite This: *ACS Energy Lett.* 2023, 8, 2042−2050

Read Online

ABSTRACT: The commercial implementation of aqueous Zn-ion batteries is being impeded by the rampant dendrite growth and exacerbated side reactions on the Zn metal anodes. Herein, a 60 nm artificial protective layer with spatial dielectric−metallic gradient composition (denoted as GZH) is developed via Zn and HfO_2 cosputtering. In this design, the top HfO_2 layer with high permittivity and low electronic conductivity effectively suppresses hydrogen evolution. The intermediate Zn-rich oxide region promotes the dendrite-free Zn deposition and reinforces the contact between Zn and the sputtered layer. This design allows stable battery operation at high currents. Symmetric cells with Zn-GZH exhibit stable voltage separation over 500 h at 10 mA cm^{-2} with a cutoff capacity of 5 mAh cm^{-2}. When paired with a vanadate cathode, the full-cell battery delivers a capacity retention of around 75% after 2000 cycles. This design concept may apply to other aqueous metal batteries.

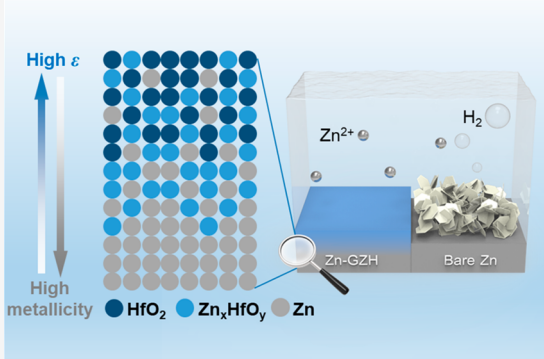

Aqueous zinc-ion batteries (AZIBs) are economically competitive in large-scale energy storage owing to their high safety and low cost. As a paramount component in AZIBs, the Zn metal anode exhibits high specific capacity (820 mAh g^{-1}), high volumetric capacity (5855 mAh cm^{-3}), and suitable operating potential in aqueous electrolyte (−0.762 V vs SHE).[1,2] Unfortunately, the commercial implementation of AZIBs is still hindered by the unsatisfactory stability of Zn metal anodes during cycling. First, the water brought by solvated Zn^{2+} leads to the spontaneous hydrogen evolution reaction (HER) on the Zn surface, which passivates the anode surface with the formation of byproducts (such as $Zn_4SO_4(OH)_6{\cdot}xH_2O$) and lowers the Zn utilization.[3,4] Second, the inhomogeneous Zn^{2+} flux during the electrodeposition process generates a "tip effect", resulting in dendrites and "dead Zn" formation.[5,6] The above issues degrade the life and efficiency of the Zn anode.

Various strategies are being employed to improve the stability of Zn metal anode, such as electrolyte optimization, hierarchical Zn host design, and artificial layer coatings.[7−12] Among them, an artificial solid-electrolyte interface on the Zn surface has proven effective in enhancing the anode reversibility. Protective layers have two major working mechanisms. The first one is to construct electronic conductive and zincophilic surfaces, such as graphene,[13] indium,[14] antimony,[15] copper,[16] silver,[17] tin,[18] and several alloys.[19−22] These interlayers provide more nucleation sites compared with bare Zn and effectively guide the uniform Zn deposition. Some 3D conductive frameworks like CNT and porous carbon were also employed to lower the local electric field and avoid concentration polarization.[23−25] However, the nucleated Zn on such surfaces cannot be further protected since the direct exposure to the electrolyte will still thermodynamically trigger HER. The other type of coating layer is composed of electronic insulating but zincophilic materials, such as polymers with abundant 3D ionic channels[26−28] and metal oxide/nitride compounds,[29,30] where the Zn plating occurs underneath the coating layer. Thus, the HER can be hindered because of reduced electron transfer to the electrolyte.[31,32] Some inorganic dielectric materials like Kaolin, ZrO_2, Si_3N_4, and

Received: February 16, 2023
Accepted: March 30, 2023
Published: April 4, 2023

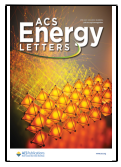

https://doi.org/10.1021/acsenergylett.3c00367
ACS Energy Lett. 2023, 8, 2042−2050

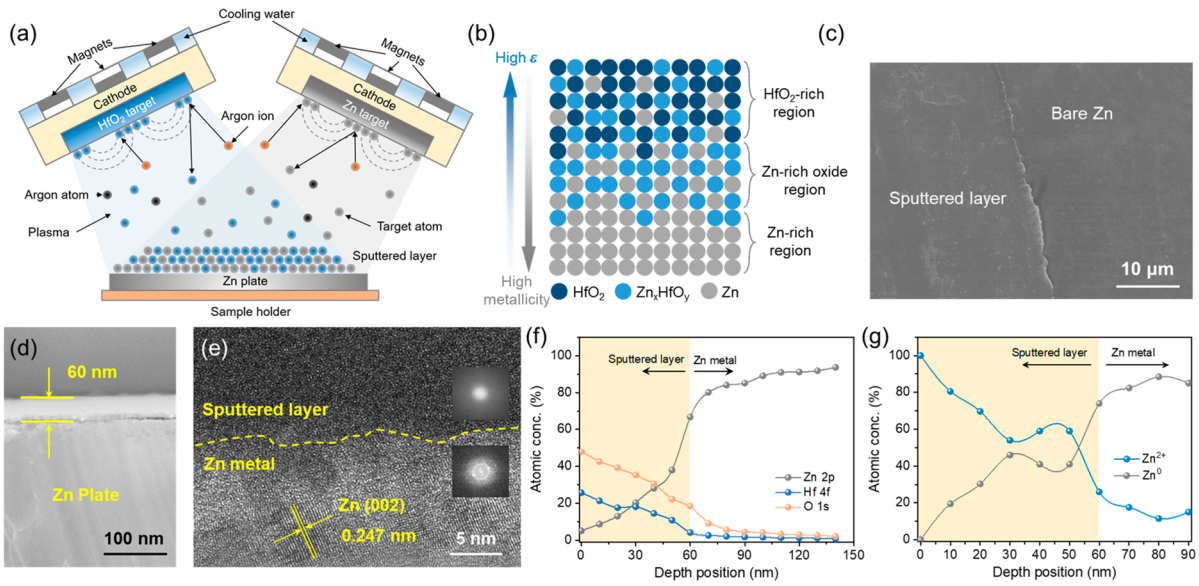

Figure 1. Fabrication and characterization of Zn-GZH. (a) Illustration of the magnetron cosputtering process on Zn metal. (b) Illustration of the composition distribution inside the Zn-GZH. (c) SEM image of Zn-GZH surface. (d) Cross-sectional SEM image of Zn-GZH after FIB milling and polishing. (e) HRTEM image of Zn-GZH and SEAD patterns (inset). (f and g) XPS depth profiles for Zn-GZH.

CeO_2 can induce Maxwell−Wagner polarization. This polarization caused by the spatial charge separation between two media with different permittivities and electrical conductivities can accelerate Zn plating and lower polarization.[33−36] Nevertheless, most of these composite layers are microscale thick and the ion-transfer kinetics are relatively low. More importantly, a rigid contact between the coatings and Zn surface is imperative to dendrite suppression and anticorrosion, especially under long-term cycling conditions.[37] Recently, a gradient host design has been successfully implemented for Zn protection (e.g., gradient porosity and gradient resistance).[38,39] Although dendrites can be eliminated by the confinement of Zn growth within the gradient pores from bottom to top, side reactions still occur on the top surface. Therefore, rational design of multilayered gradients is of significance for the design of a protective layer on the Zn anode.

HfO_2 is widely used as a high-permittivity (k) gate insulator in field-effect transistors, and it can be easily fabricated by sputtering, atomic layer deposition, and chemical vapor deposition processes.[40] Accordingly, it is proposed that a nano-scaled HfO_2 thin film should be an effective anticatalyst for HER at metal anodes in aqueous electrolyte solutions. Herein, to synergistically combine the advantages of the ionic conductive and electronic insulating artificial protective layers, a dielectric−metallic double-gradient design strategy is proposed with the assistance of magnetron cosputtering technology. By controlling the sputtering power of target Zn and HfO_2, a relatively thin (∼60 nm) coating layer with an HfO_2 enriched surface is obtained and the content of metallic Zn increases with depth (abbreviated as Zn-GZH). The intermediate region shows a progressive composition transition with the formation of zinc-doped HfO_2 (Zn_xHfO_y). The outermost HfO_2 with a high dielectric constant (∼25, Figure S1) and high breakdown voltage could efficiently block the electron pathway and thereby reduce the HER tendency. The inside Zn_xHfO_y with a Zn^{2+} conductivity higher than that of HfO_2 could uniformize the Zn^{2+} flux and eliminate the "tip effect". The large contact area with a strong interfacial binding energy between metallic Zn and Zn_xHfO_y guarantees sufficient adhesion of the sputtered layer on Zn and simultaneously lowers the electrical field density, further guiding a homogeneous Zn nucleation process without corrosion. With this design, the Zn-GZH symmetric cells exhibit a low and stable voltage polarization over 1400 h at 1 mA cm^{-2} with a capacity of 1 mAh cm^{-2}. In addition, an outstanding Zn plating/stripping reversibility has been realized with a high Coulombic efficiency (CE) of around 99.9% after 3000 cycles at 5 mA cm^{-2} in Zn||Ti-GZH. The full cell based on a vanadate cathode and the Zn-GZH anode can cycle for 2000 cycles with a capacity retention of over 75% at 5 A g^{-1}. This effective dielectric−metallic film protection design broadens the perspective for the development of stable and high-performance AZIBs.

The fabrication process of Zn-GZH is schematically presented in Figure 1a. A polished Zn plate was placed in the chamber of a magnetron sputtering system equipped with Zn and HfO_2 targets. To obtain the gradient structure, the radio frequency power for the HfO_2 target was fixed while that of the Zn target gradually reduced throughout the deposition (Experimental Section and Figure S2). The as-prepared Zn-GZH is expected to have an HfO_2-rich surface and a Zn-rich oxide region inside with the increased content of Zn metal (Figure 1b). The Zn plate surface remains smooth after sputtering without tip formation (Figure 1c), indicating that the sputtered layer is uniform and dense. The X-ray diffraction (XRD) pattern demonstrates that no crystalline phase is introduced after GZH coating (Figure S3a). Similarly, pure HfO_2 coverage on the Zn plate can also be obtained (denoted as Zn-H, Figure S4), if the sputtering was carried out with a fixed power of a single HfO_2 target. Digital photographs show that the sputtering process does not influence the macroscopic morphology of the Zn plate, except for the color change by differeent content of HfO_2 (Figure S3b).

The thickness of the sputtered GZH layer and the interface with the Zn substrate are investigated. The thickness of GZH is around 60 nm as determined by atomic force microscopy depth profile and cross-sectional scanning electron microscopy (SEM) images of the Zn-GZH after FIB cutting (Figures 1d,

https://doi.org/10.1021/acsenergylett.3c00367
ACS Energy Lett. 2023, 8, 2042−2050

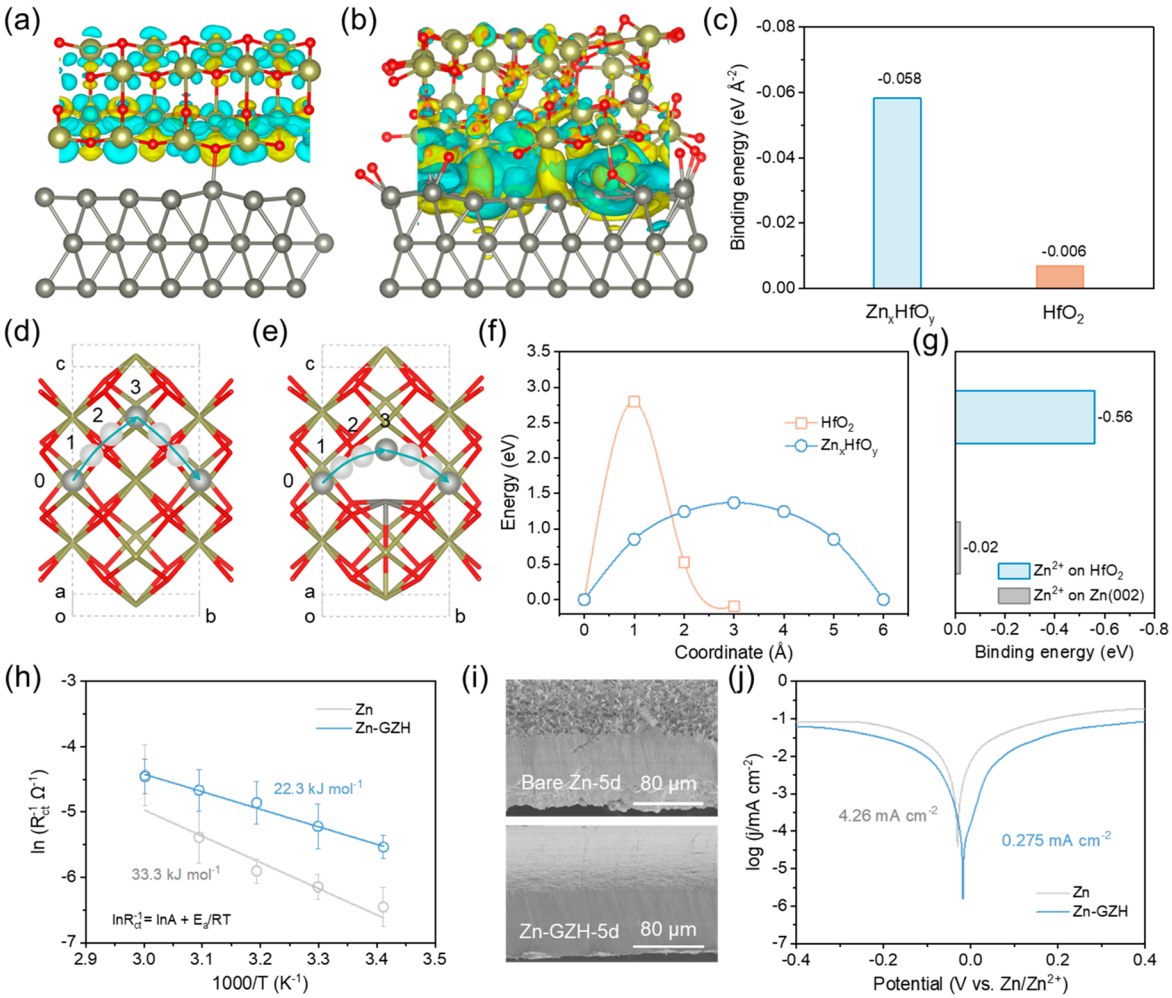

Figure 2. Zn redox kinetics and anticorrosion behavior of Zn-GZH. Optimized structures and charge density difference distributions of (a) Zn-HfO_2 and (b) Zn-Zn_xHfO_y interface. (c) Calculated binding energies of Zn-HfO_2 and Zn-Zn_xHfO_y interface. (d−f) Calculations of the optimum Zn^{2+} diffusion pathway in HfO_2 and Zn_xHfO_y. (g) Calculated binding energies for a foreign Zn^{2+} on HfO_2 and bare Zn surface. (h) Arrhenius curves and activation energies of Zn deposition. (i) Cross-sectional SEM images of electrode surfaces after 5 days of immersion in 2 M $ZnSO_4$ electrolyte. (j) Linear polarization curves.

S5, and S6). Compared with the previously reported microthickness metal oxide compound protective layers with high dielectric constants (Figure S1), the thinner GZH will benefit the kinetics of aqueous batteries. A close contact between the amorphous GZH and crystalline Zn metal is observed in the cross-sectional TEM images (Figure 1e and the SEAD patterns inset). TEM-EDS mapping images and element analysis (Figure S7) show a clear boundary between Zn and Hf distribution in Zn-H while the interface in Zn-GZH is obscured, indicating the compositional gradient of Zn content in GZH.

To better quantify the composition of the GZH layer, X-ray photoelectron spectra (XPS) depth profiles were collected with the assistance of Ar etching. It is found that the atomic concentrations of both O and Hf decline while the concentration of Zn increases down to the depth of 60 nm (Figure 1f). From the spectra of Zn 2p and Hf 4f (Figures 1g and S8), the intensities of the Zn^{2+} peaks decrease with the growth of defective HfO_2, suggesting that HfO_2 was successfully doped by Zn^{2+} during the cosputtering process. Hence, it is inferred that the outermost surface of the GZH layer is mainly composed of HfO_2, followed by a Zn_xHfO_y intermediate layer and a bottom region of metallic Zn (Figure 1b).

During Zn plating and stripping, the interfacial site between the protective layer and the Zn surface undergoes a cyclic dynamic destruction and reconstruction process. Hence, a rigid interface and strong adhesion is important to the cycle stability. Artificial interlayers with poor adhesion to Zn will peel off after several cycles.[41] To verify the interaction between the sputtered GZH layer and Zn metal, density functional theory (DFT) calculations were performed. Rich Zn−O bonds are formed between Zn and Zn_xHfO_y (Figures 2a,b and S9), which is supported by the obvious charge transfer and redistribution at the interface where electrons transfer from Zn metal to the electronegative O. As shown in Figure 2c, the Zn−O bond enriched interface displays a much stronger binding energy (58 meV Å^{-2}) than that between Zn and pure HfO_2 with less Zn−O coupling (6 meV Å^{-2}).

In addition to interface adhesion, efficient Zn ion transport through the protective layer is also essential to ensure dendrite-free nucleation. According to the simulated Zn^{2+} pathways in HfO_2 and Zn_xHfO_y (Figure 2d,e), the HfO_2 framework with partial Hf substituted by low-valence Zn could broaden pathways for guest Zn^{2+} migration.[42] As a result, the calculated

https://doi.org/10.1021/acsenergylett.3c00367
ACS Energy Lett. 2023, 8, 2042−2050

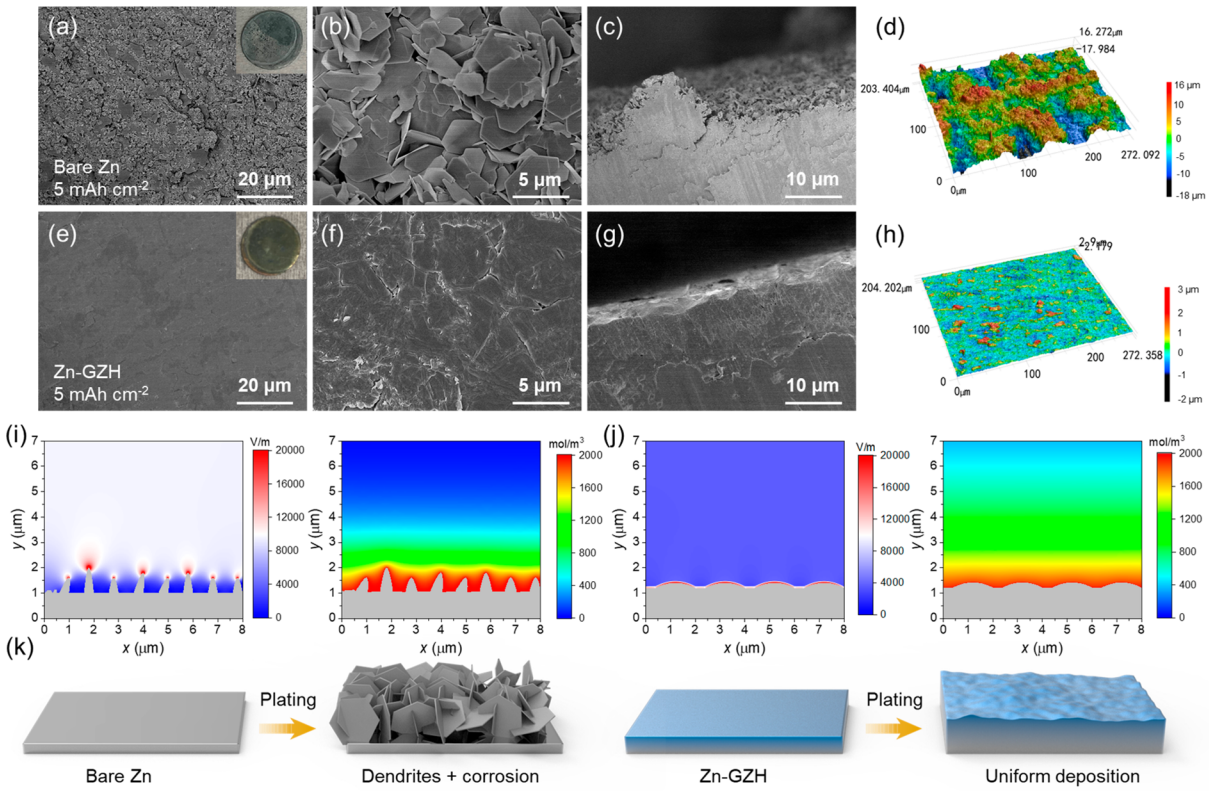

Figure 3. Zn deposition and dendrites growth behaviors. SEM images of (a−c) bare Zn and (e−g) Zn-GZH after Zn deposition with a capacity of 5 mAh cm^{-2} (insets: digital photographs). CLSM 3D topography images of (d) bare Zn and (h) Zn-GZH after deposition. The simulation of electric field distribution and ionic flux distribution for (i) bare Zn and (j) Zn-GZH. (k) Schematics of the Zn precipitation on bare Zn and Zn-GZH surface.

diffusion barrier for Zn^{2+} in Zn_xHfO_y is 1.36 eV (Figure 2f), much lower than that in pure HfO_2 (2.76 eV). To evaluate the zincophilicity of the outmost region of the GZH layer, the adsorption energies of a foreign Zn^{2+} on Zn(002) and HfO_2 were also studied (Figure S10). As shown in Figure 2g, HfO_2 presents a much stronger Zn^{2+} immobilization capability than bare Zn (∼30 times), indicating that GZH coating is favorable for Zn^{2+} capture. Such a property was also supported by the lower contact angles of $ZnSO_4$ electrolyte on Zn-H and Zn-GZH compared with bare Zn (Figure S11).

The activation energy (E_a) of Zn^{2+} desolvation is a key parameter of reaction kinetics, which is quantitively measured based on the temperature-dependent electrochemical impedance spectra (EIS).[43] As presented in Figures 2h and S12, according to the Arrhenius equation, the E_a on Zn-GZH is 22.3 kJ mol^{-1}, smaller than that on bare Zn (33.3 kJ mol^{-1}), indicating a promoted desolvation process on Zn-GZH.

To investigate the anticorrosion effect of the GZH layer, samples of bare Zn, Zn-H, and Zn-GZH were immersed in 2 M $ZnSO_4$ solution and rested for 5 days. Hexagonal microsheets with random orientation are found on bare Zn (Figure 2i and S13a). In contrast, Zn-H and Zn-GZH maintain a flat surface after soaking (Figures 2i and S13b,c). EDS element mapping images and spectra (Figure S13d,e) reveal the sulfur presence in the flakes covered on Zn, which is further identified as zinc hydroxide sulfate hydrate ($Zn_4SO_4(OH)_6{\cdot}5H_2O$, ZSH) from the XRD pattern (Figure S13f). The formation of ZSH is assigned to the high pH value of the electrolyte near the Zn surface, which is caused by the consumption of H^+ in the HER process.[31] For Zn-GZH, the HfO_2 located on the surface could block the electron transfer and further leads to a low HER tendency with little ZSH formation.

The anticorrosion behavior on the GZH layer was further analyzed by the linear polarization measurements (Figure 2j). The Zn-GZH exhibits a higher corrosion potential and a lower corrosion current density (0.275 mA cm^{-2}) than that of bare Zn (4.260 mA cm^{-2}), implying a retarded corrosion rate.[44] From the linear sweep voltammetry (LSV) curve in the Na_2SO_4 solution (Figure S14a), the hydrogen evolution potential on Zn-GZH is more negative than that of bare Zn. Additionally, the Gibbs free energy of hydrogen adsorption on HfO_2 is about 1.36 eV, higher than that on bare Zn (Figure S14b), reflecting a hard occurrence of HER on Zn-GZH.[45] The above experimental and simulation results verify that the hydrogen-involved surface corrosion on Zn metal has been efficiently prevented by the sputtered GZH layer.

The morphological evaluation of the Zn plating on different samples was carried out with a current density of 1 mA cm^{-2} and an areal capacity of 5 mAh cm^{-2}. As shown in Figures 3a−c and S15a,b, loose Zn dendrites with sharp edges are found on bare Zn. In contrast, Zn-GZH shows a dense and flat surface (Figure 3e-g and S15c-d). The height measurement collected by confocal laser scanning microscope (CLSM) demonstrates that the surface roughness (developed surface area ratio, S_{dr}) of bare Zn after Zn deposition is much higher than that on Zn-GZH (4.65 vs 0.89, Figure 3d and 3h, Figure S16). It is worth noting that significant crack formation and delamination are observed between Zn and pure HfO_2 sputtered layer (Figure S17), which could be attributed to the poor binding energy of

https://doi.org/10.1021/acsenergylett.3c00367
ACS Energy Lett. 2023, 8, 2042−2050

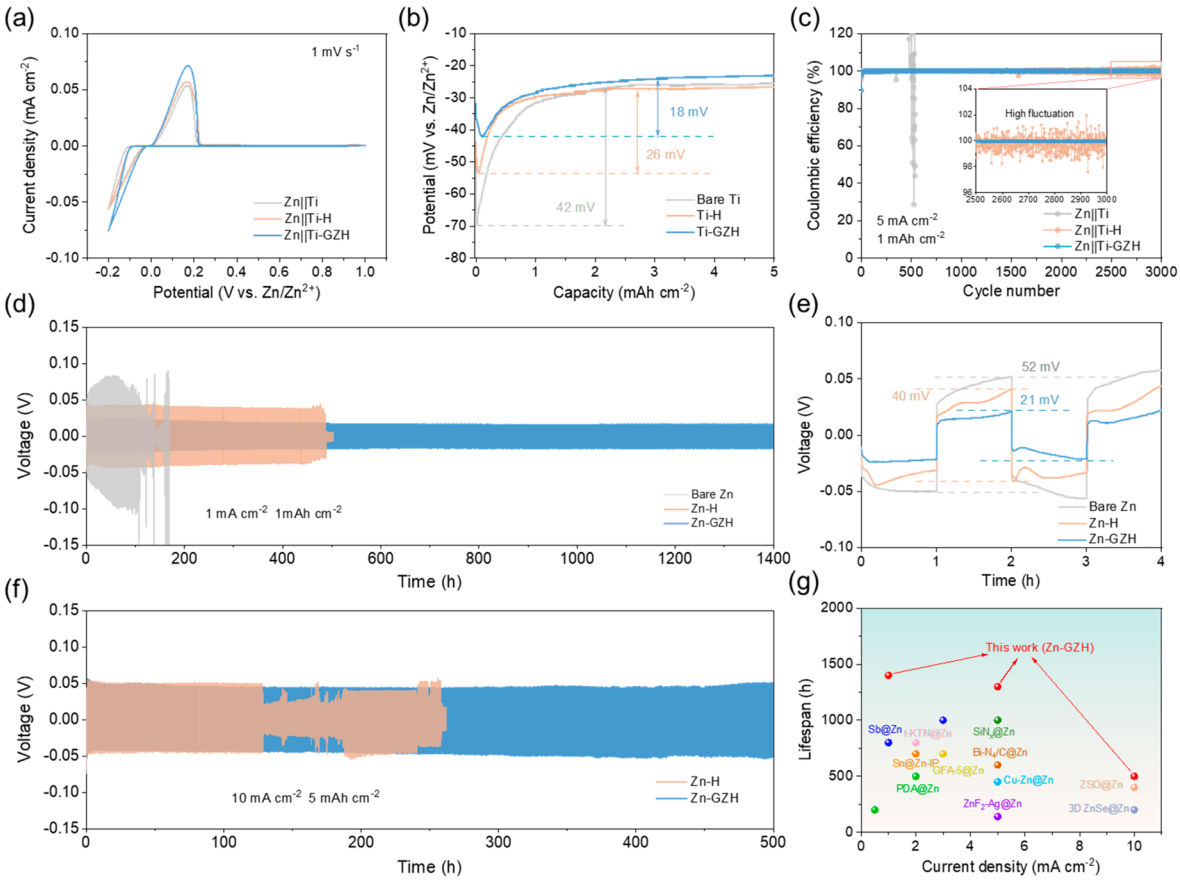

Figure 4. Reversibility and stability of Zn plating/stripping. (a) CV curves. (b) Nucleation overpotential and (c) CE of Zn plating/stripping. Long-term galvanostatic cycling of symmetric Zn cells (d) 1 mA cm^{-2}, 1 mAh cm^{-2}, (e) selected cycles in panel d, and (f) 10 mA cm^{-2}, 5 mAh cm^{-2}. (g) Comparison of cycle performance and current density of the Zn-GZH with some previously reported anodes.

pure HfO_2 on Zn, as well as the limited Zn^{2+} transport in HfO_2. More visual evidence for the suppression of dendrite growth on Zn-GZH is given by in situ optical microscopy observation (Figure S18a,b). After depositing at 0.5 mA cm^{-2} for 1 h, bare Zn was completely covered by discernible clusters of dendrites, while the Zn-GZH surface remains nearly intact. EDS mapping images of Hf, O, and Zn on Zn-GZH after Zn precipitation corroborate that the GZH layer still tightly anchors on the Zn plate (Figure S18c).

To unveil the underlying mechanism for the Zn nucleation behavior, chronoamperometry (CA) curves at an overpotential of −200 mV were examined (Figure S18d). The current densities on both bare Zn and Zn-H keep increasing for over 200 s, which can be explained by a random diffusion on the tips.[46] As shown before, the GZH layer adheres to Zn tightly via Zn−O bonds, which constrain the 2D Zn^{2+} lateral diffusion and guide uniform nucleation with steady current density. According to the simulation by the finite element method (Figure 3i,j), a highly localized electric field surrounds the nucleated Zn tips with a significant intensity gradient on bare Zn, while a more homogeneous electric field can be achieved on Zn-GZH. Similarly, the uneven Zn^{2+} distribution on bare Zn propels the charge accumulation and promotes the nucleation onto the specific tip sites. In contrast, GZH coverage delivers a low concentration gradient of Zn^{2+}, ensuring a smooth surface during Zn plating.[47] The Zn plating process on bare Zn, Zn-H, and Zn-GZH is schematically presented in Figures 3k and S17.

To demonstrate the merits of the GZH layer in terms of kinetic advantages, Zn plating/stripping was conducted on Ti foil first. The cyclic voltammetry (CV) curves present typical cathodic loops and anodic peaks on both bare Ti, Ti−H, and Ti-GZH electrodes (Figure 4a). Notably, with the GZH layer on a Ti foil, a shorter delay of cathodic current with a higher peak current compared with bare Ti and Ti−H indicates a reduced Zn deposition barrier.[43] Similar phenomena can also be observed in discharge voltage profiles at 1 mA cm^{-2} with 5 mAh cm^{-2} (Figure 4b). The nucleation of Zn on GZH-Ti shows a lower overpotential (18 mV) than that on Ti−H (26 mV) and bare Ti (42 mV). Benefiting from the facilitated kinetics and anticorrosion effect of GZH, a high Coulombic efficiency (CE) of around 99.2% is attained after cycling at 1 mA cm^{-2} with a fixed capacity of 1 mAh cm^{-2} (Figure S19a−c). As a comparison, the voltage drops substantially after 100 cycles for the Zn||Ti cell, because of the short initiated by dendrite growth. Even with a higher current density of 5 mA cm^{-2} (Figure 4c), Ti-GZH still maintains a high CE value of around 99.9% with low fluctuation after 3000 cycles, illustrating that Zn plating/stripping is highly reversible with the aid of GZH coverage.

The impact of the sputtered GZH layer on Zn anode improvement was further validated in Zn||Zn symmetric cells. At 1 mA cm^{-2} with a capacity of 1 mAh cm^{-2}, the failure of the cells with bare Zn and Zn-H happens within 500 h (Figure 4d). However, the cell with Zn-GZH exhibits a stable potential separation up to 1400 h. Moreover, in accordance with the

https://doi.org/10.1021/acsenergylett.3c00367
ACS Energy Lett. 2023, 8, 2042−2050

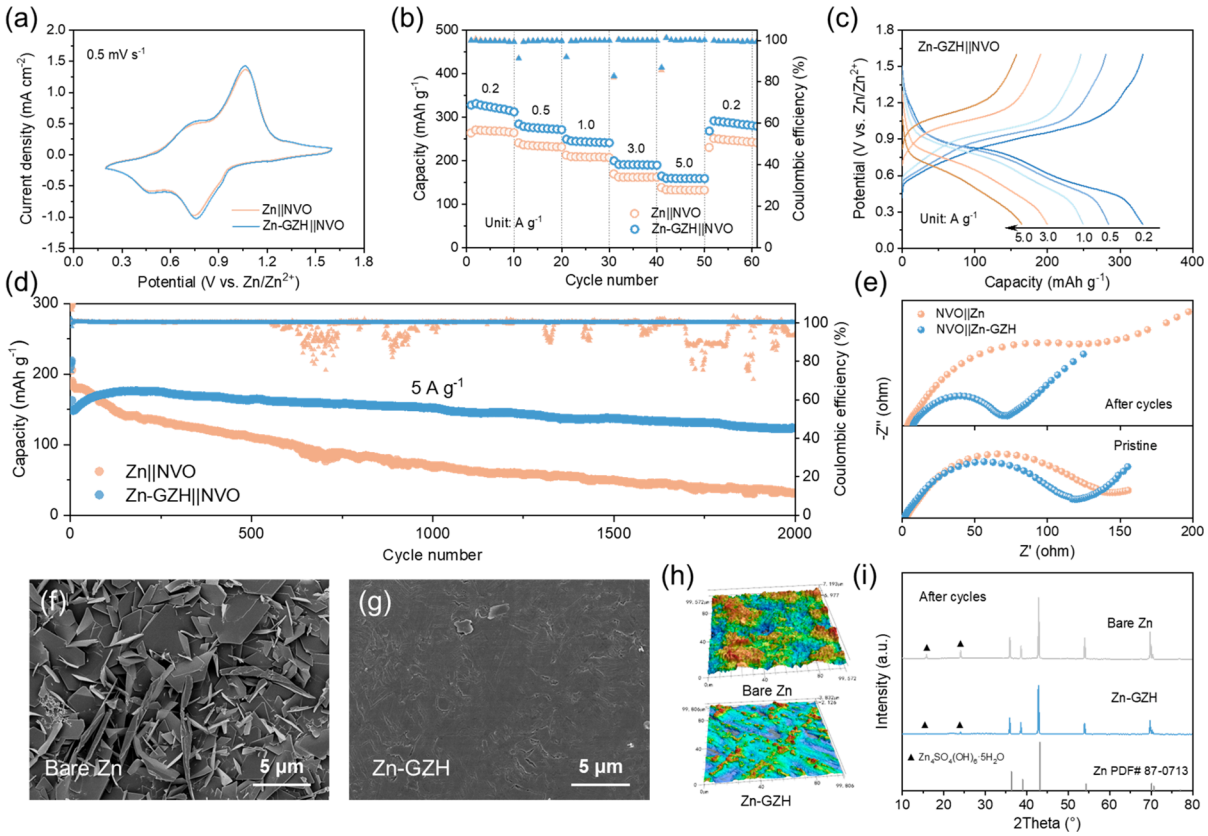

Figure 5. Validation in full cells. (a) CV curves. (b) Rate performance and (c) the corresponding charge−discharge curves. (d) Cycling performance at a current density of 5 A g^{-1} and the (e) EIS spectra of the cells before and after 5 A g^{-1} cycling. (f and g) SEM images, (h) CLSM 3D height images, and (i) XRD patterns of bare Zn and Zn-GZH electrodes after long-term cycling.

previous reaction kinetics analysis on the Zn||Ti cell, the polarization of Zn redox on Zn-GZH (21 mV) is lower than that on Zn-H (40 mV) and bare Zn (52 mV) (Figure 4e). The lower overpotential of Zn plating on Zn-GZH could be attributed to the lower desolvation barrier and more Zn transport channels compared with bare Zn and Zn-H. When the current density increases to 5 and 10 mA cm^{-2} (Figures S19d and 4f), stable cycling performance without electrical short can still be realized in the cells with Zn-GZH over 1300 and 500 h, respectively. Meanwhile, the pure HfO_2 layer on Zn-H with poor adhesion quickly loses its function, which could be related to delamination and crack formation. To be more specific, poor binding and limited contact area between pure HfO_2 and Zn will lead to formation of microcracks during the stripping/plating process. At the crack area, the subsequent Zn nucleation and dissolution readily occur on the exposed Zn metal,[37] leading to aggravated side reactions, dendrite growth, and delamination of the HfO_2 layer. The rate performance measurement shows that Zn-GZH can possess a lower and more stable voltage hysteresis at currents ranging from 0.5 to 20 mA cm^{-2} (Figure S19e). The electrochemical performance of Zn-GZH is superior to the recently reported Zn protective layers under mildly acidic conditions (Figure 4g).[9,15,17,20,47−53] According to the previous analyses, the improvement of electrode stability by the dielectric−metallic ultrathin film can be attributed to the intrinsic high permittivity, high breakdown voltage, and good interfacial compatibility, which can effectively block the electron pathways, reduce side reactions, and further ensure electrochemical reversibility.[54]

The advantage of the Zn-GZH anode was further validated in full cells paired with a sodium vanadate ($Na_2V_6O_{16}\cdot 1.63H_2O$, NVO) cathode (Figure S20). The CV curves at the scan rate of 0.5 mV s^{-1} of Zn||NVO and Zn-GZH||NVO devices both exhibit two couples of redox peaks (Figure 5a), corresponding to the Zn^{2+}/H^+ co-insertion and extraction process.[55,56] The Zn-GZH||NVO device retains high specific capacities when the current varies from 0.2 to 5.0 A g^{-1} (Figure 5b,c). Due to the electrochemical excellence of the GZH layer, the Zn-GZH||NVO full cell delivers a capacity of around 254.7 mAh g^{-1} after 500 cycles at 1 A g^{-1}, which is over twice that of Zn||NVO (Figure S20c). The elevated capacity stability is also demonstrated at a higher current density of 5 A g^{-1}, with a capacity retention of 75.3% capacity after 2000 cycles. In contrast, the cell with bare Zn anode deteriorates rapidly after 500 cycles with a severe CE fluctuation. This enhanced cycle stability stems from the stable Zn anode surface with much less side reactions on the Zn-GZH anode. It is observed that transfer resistance of the Zn-GZH||NVO cell drops after cycles (Figure 5e), which may be related to the activation process of the cathode due to deep electrolyte infiltration during cycles.[57]

To gain insight into the full cell performance improvement, the surface morphologies of bare Zn and Zn-GZH anodes after cycling at 5 A g^{-1} were evaluated. As demonstrated in Figure 5f,g, harsh flake-like Zn dendrites are found on bare Zn, while the cycled Zn-GZH anode remains intact. The 3D height images also evidence the high roughness of the bare Zn plate after the full cell test (Figures 5h and S21), and the S_{dr} is reduced to 0.57 on Zn-GZH anode, much lower than that on bare Zn (4.37). The XRD patterns indicate that ZSH

https://doi.org/10.1021/acsenergylett.3c00367
ACS Energy Lett. 2023, 8, 2042−2050

accumulates more significantly on bare Zn than on Zn-GZH during cycling (Figure 5i). The above results show that bare Zn suffers dendrite growth and HER during the charge/discharge process in full cells. Arising from the loose compact of dendrites and ZSH sheets, the tip effect will be aggravated together with the H_2O decomposition.[58] Consequently, more ZSH will be generated and passivate the surface, leading to fast capacity decay and poor rate performance. Simultaneously, the disordered dendrites will penetrate through the separator and reach the cathode, resulting in a short circuit in the battery.

In summary, an ultrathin and uniform artificial Zn anode protective layer with dielectric−metallic double-gradient composition has been realized. In this design, this gradient structure synergistically exerts the merits of the electronic insulating layer and the ionic conductive layer. First, the outermost dielectric HfO_2 efficiently lowers the HER tendency. The mixture of Zn and Zn_xHfO_y filling in the subsurface with a progressive increase of metallic Zn content constructs a large interfacial area, which further regulates Zn^{2+} flux and guarantees a uniform electric field distribution. Second, a strong interface adhesion via Zn−O bonding maintains the mechanical stability and eliminates delamination and crack formation. As expected, the as-fabricated Zn-GZH anode exhibits a dendrite-free morphology and low HER corrosion tendency. As a result, the full battery can cycle up to 2000 cycles with capacity retention of 75%. This gradient design strategy could pave the way for the development of dendrite-free metal anodes and accelerate the commercial implementation of stable aqueous batteries.

■ ASSOCIATED CONTENT

Supporting Information

The Supporting Information is available free of charge at https://pubs.acs.org/doi/10.1021/acsenergylett.3c00367.

Figures S1−S21, additional characterizations of samples and electrochemical measurements; atomic models for DFT calculation (PDF)

■ AUTHOR INFORMATION

Corresponding Authors

Peihua Yang − *The Institute of Technological Sciences, MOE Key Laboratory of Hydrodynamic Transients, Wuhan University, Wuhan 430072, China;* orcid.org/0000-0003-0178-6896; Email: peihua.yang@whu.edu.cn

Hong Jin Fan − *School of Physical and Mathematical Sciences, Nanyang Technological University, Singapore 637371, Singapore;* orcid.org/0000-0003-1237-4555; Email: fanhj@ntu.edu.sg

Authors

Jin-Lin Yang − *School of Physical and Mathematical Sciences, Nanyang Technological University, Singapore 637371, Singapore;* orcid.org/0000-0002-5722-3948

Lingli Liu − *School of Physical and Mathematical Sciences, Nanyang Technological University, Singapore 637371, Singapore;* orcid.org/0000-0002-4360-2699

Zehua Yu − *The Institute of Technological Sciences, MOE Key Laboratory of Hydrodynamic Transients, Wuhan University, Wuhan 430072, China*

Pengbo Chen − *The Institute of Technological Sciences, MOE Key Laboratory of Hydrodynamic Transients, Wuhan University, Wuhan 430072, China*

Jia Li − *Rolls-Royce@NTU Corporate Lab, Nanyang Technological University, Singapore 639798, Singapore;* orcid.org/0000-0002-5433-1521

Putu Andhita Dananjaya − *School of Physical and Mathematical Sciences, Nanyang Technological University, Singapore 637371, Singapore;* orcid.org/0000-0001-9416-6455

Eng Kang Koh − *School of Physical and Mathematical Sciences, Nanyang Technological University, Singapore 637371, Singapore;* orcid.org/0000-0003-0733-7688

Wen Siang Lew − *School of Physical and Mathematical Sciences, Nanyang Technological University, Singapore 637371, Singapore;* orcid.org/0000-0002-5161-741X

Kang Liu − *The Institute of Technological Sciences, MOE Key Laboratory of Hydrodynamic Transients, Wuhan University, Wuhan 430072, China;* orcid.org/0000-0002-2781-2581

Complete contact information is available at: https://pubs.acs.org/10.1021/acsenergylett.3c00367

Author Contributions

[#]J.-L.Y. and L.L. contributed equally to this work. H.J.F. and P.Y. conceived the research. J.-L.Y. designed and performed the experiments, performed characterization of the materials, and analyzed the data. L.L., E.K.K., P.A.D., and W.S.L. participated in magnetron sputtering. Z.Y. and P.C. conducted the theoretical simulations. J.-L.Y., J.L., and L.L. wrote the manuscript, and all authors reviewed and revised the manuscript.

Notes

The authors declare no competing financial interest.

■ ACKNOWLEDGMENTS

P.Y. acknowledges the National Natural Science Foundation of China (22209124). H.J.F. acknowledges financial support from the Singapore Ministry of Education by Tier 2 (MOE-T2EP50121-0006). J.-L.Y. is thankful for the financial support by the China Scholarship Council (No. 202006210070). The authors appreciate the Supercomputing Center of Wuhan University for numerical calculations supporting.

■ REFERENCES

(1) Ruan, P.; Liang, S.; Lu, B.; Fan, H. J.; Zhou, J. Design Strategies for High-Energy-Density Aqueous Zinc Batteries. *Angew. Chem., Int. Ed.* **2022**, *61*, No. e202200598.

(2) Li, C.; Jin, S.; Archer, L. A.; Nazar, L. F. Toward Practical Aqueous Zinc-Ion Batteries for Electrochemical Energy Storage. *Joule* **2022**, *6*, 1733−1738.

(3) Yang, J.; Yin, B.; Sun, Y.; Pan, H.; Sun, W.; Jia, B.; Zhang, S.; Ma, T. Zinc Anode for Mild Aqueous Zinc-Ion Batteries: Challenges, Strategies, and Perspectives. *Nano-Micro Lett.* **2022**, *14*, 42.

(4) Yang, W.; Yang, Y.; Yang, H.; Zhou, H. Regulating Water Activity for Rechargeable Zinc-Ion Batteries: Progress and Perspective. *ACS Energy Lett.* **2022**, *7*, 2515−2530.

(5) Qin, R.; Wang, Y.; Yao, L.; Yang, L.; Zhao, Q.; Ding, S.; Liu, L.; Pan, F. Progress in Interface Structure and Modification of Zinc Anode for Aqueous Batteries. *Nano Energy* **2022**, *98*, 107333.

(6) Zuo, Y.; Wang, K.; Pei, P.; Wei, M.; Liu, X.; Xiao, Y.; Zhang, P. Zinc Dendrite Growth and Inhibition Strategies. *Mater. Today Energy* **2021**, *20*, 100692.

(7) Zhao, K.; Fan, G.; Liu, J.; Liu, F.; Li, J.; Zhou, X.; Ni, Y.; Yu, M.; Zhang, Y. M.; Su, H.; Liu, Q.; Cheng, F. Boosting the Kinetics and Stability of Zn Anodes in Aqueous Electrolytes with Supramolecular Cyclodextrin Additives. *J. Am. Chem. Soc.* **2022**, *144*, 11129−11137.

(8) Yang, J.-L.; Yang, P.; Yan, W.; Zhao, J.-W.; Fan, H. J. 3D Zincophilic Micro-Scaffold Enables Stable Zn Deposition. *Energy Storage Mater.* **2022**, *51*, 259−265.
(9) Peng, H.; Fang, Y.; Wang, J.; Ruan, P.; Tang, Y.; Lu, B.; Cao, X.; Liang, S.; Zhou, J. Constructing Fast-Ion-Conductive Disordered Interphase for High-Performance Zinc-Ion and Zinc-Iodine Batteries. *Matter* **2022**, *5*, 4363−4378.
(10) Zhou, J.; Wu, F.; Mei, Y.; Hao, Y.; Li, L.; Xie, M.; Chen, R. Establishing Thermal Infusion Method for Stable Zinc Metal Anodes in Aqueous Zinc-Ion Batteries. *Adv. Mater.* **2022**, *34*, 2200782.
(11) Yang, P.; Yang, J.-L.; Liu, K.; Fan, H. J. Hydrogels Enable Future Smart Batteries. *ACS Nano* **2022**, *16*, 15528−15536.
(12) Qiu, M.; Sun, P.; Wang, Y.; Ma, L.; Zhi, C.; Mai, W. Anion-Trap Engineering toward Remarkable Crystallographic Reorientation and Efficient Cation Migration of Zn Ion Batteries. *Angew. Chem., Int. Ed.* **2022**, *61*, No. e202210979.
(13) Zhou, J.; Xie, M.; Wu, F.; Mei, Y.; Hao, Y.; Huang, R.; Wei, G.; Liu, A.; Li, L.; Chen, R. Ultrathin Surface Coating of Nitrogen-Doped Graphene Enables Stable Zinc Anodes for Aqueous Zinc-Ion Batteries. *Adv. Mater.* **2021**, *33*, 2101649.
(14) Xiao, P.; Li, H.; Fu, J.; Zeng, C.; Zhao, Y.; Zhai, T.; Li, H. An Anticorrosive Zinc Metal Anode with Ultra-Long Cycle Life Over One Year. *Energy Environ. Sci.* **2022**, *15*, 1638−1646.
(15) Hong, L.; Wang, L. Y.; Wang, Y.; Wu, X.; Huang, W.; Zhou, Y.; Wang, K. X.; Chen, J. S. Toward Hydrogen-Free and Dendrite-Free Aqueous Zinc Batteries: Formation of Zincophilic Protective Layer on Zn Anodes. *Adv. Sci.* **2022**, *9*, 2104866.
(16) Zhou, L.; Yang, F.; Zeng, S.; Gao, X.; Liu, X.; Cao, X.; Yu, P.; Lu, X. Zincophilic Cu Sites Induce Dendrite-Free Zn Anodes for Robust Alkaline/Neutral Aqueous Batteries. *Adv. Funct. Mater.* **2022**, *32*, 2110829.
(17) Wang, D.; Lv, D.; Peng, H.; Wang, N.; Liu, H.; Yang, J.; Qian, Y. Site-Selective Adsorption on ZnF_2/Ag Coated Zn for Advanced Aqueous Zinc-Metal Batteries at Low Temperature. *Nano Lett.* **2022**, *22*, 1750−1758.
(18) Zhou, M.; Fu, C.; Qin, L.; Ran, Q.; Guo, S.; Fang, G.; Lang, X.; Jiang, Q.; Liang, S. Intrinsic Structural Optimization of Zinc Anode with Uniform Second Phase for Stable Zinc Metal Batteries. *Energy Storage Mater.* **2022**, *52*, 161−168.
(19) Tian, H.; Li, Z.; Feng, G.; Yang, Z.; Fox, D.; Wang, M.; Zhou, H.; Zhai, L.; Kushima, A.; Du, Y.; Feng, Z.; Shan, X.; Yang, Y. Stable, High-Performance, Dendrite-Free, Seawater-Based Aqueous Batteries. *Nat. Commun.* **2021**, *12*, 237.
(20) Li, B.; Yang, K.; Ma, J.; Shi, P.; Chen, L.; Chen, C.; Hong, X.; Cheng, X.; Tang, M. C.; He, Y. B.; Kang, F. Multicomponent Copper-Zinc Alloy Layer Enabling Ultra-Stable Zinc Metal Anode of Aqueous Zn-ion Battery. *Angew. Chem., Int. Ed.* **2022**, *61*, No. e202212587.
(21) Wang, L.; Huang, W.; Guo, W.; Guo, Z. H.; Chang, C.; Gao, L.; Pu, X. Sn Alloying to Inhibit Hydrogen Evolution of Zn Metal Anode in Rechargeable Aqueous Batteries. *Adv. Funct. Mater.* **2022**, *32*, 2108533.
(22) Zheng, J.; Huang, Z.; Zeng, Y.; Liu, W.; Wei, B.; Qi, Z.; Wang, Z.; Xia, C.; Liang, H. Electrostatic Shielding Regulation of Magnetron Sputtered Al-Based Alloy Protective Coatings Enables Highly Reversible Zinc Anodes. *Nano Lett.* **2022**, *22*, 1017−1023.
(23) Xu, Z.; Jin, S.; Zhang, N.; Deng, W.; Seo, M. H.; Wang, X. Efficient Zn Metal Anode Enabled by O,N-Codoped Carbon Microflowers. *Nano Lett.* **2022**, *22*, 1350−1357.
(24) Park, J. B.; Choi, C.; Park, J. H.; Yu, S.; Kim, D. W. Synergistic Design of Multifunctional Interfacial Zn Host toward Practical Zn Metal Batteries. *Adv. Energy Mater.* **2022**, *12*, 2202937.
(25) Wang, H.; Chen, Y.; Yu, H.; Liu, W.; Kuang, G.; Mei, L.; Wu, Z.; Wei, W.; Ji, X.; Qu, B.; Chen, L. A Multifunctional Artificial Interphase with Fluorine-Doped Amorphous Carbon layer for Ultra-Stable Zn Anode. *Adv. Funct. Mater.* **2022**, *32*, 2205600.
(26) Vijayakumar, V.; Ghosh, M.; Kurian, M.; Torris, A.; Dilwale, S.; Badiger, M. V.; Winter, M.; Nair, J. R.; Kurungot, S. An In Situ Cross-Linked Nonaqueous Polymer Electrolyte for Zinc-Metal Polymer Batteries and Hybrid Supercapacitors. *Small* **2020**, *16*, 2002528.
(27) Dilwale, S.; Ghosh, M.; Vijayakumar, V.; Kurungot, S. Electrodeposited Layered Sodium Vanadyl Phosphate ($Na_xVOPO_4 \cdot nH_2O$) as Cathode Material for Aqueous Rechargeable Zinc Metal Batteries. *Energy Fuels* **2022**, *36*, 6520−6531.
(28) Vijayakumar, V.; Torris, A.; Kurian, M.; Mathew, M. M.; Ghosh, M.; Khairnar, A. B.; Badiger, M. V.; Kurungot, S. A Sulfonated Polyvinyl Alcohol Ionomer Membrane Favoring Smooth Electrodeposition of Zinc for Aqueous Rechargeable Zinc Metal Batteries. *Sustainable Energy Fuels* **2021**, *5*, 5557−5564.
(29) Liu, Y.; Guo, T.; Liu, Q.; Xiong, F.; Huang, M.; An, Y.; Wang, J.; An, Q.; Liu, C.; Mai, L. Ultrathin ZrO_2 Coating Layer Regulates Zn Deposition and Raises Long-Life Performance of Aqueous Zn Batteries. *Mater. Today Energy* **2022**, *28*, 101056.
(30) Li, J.; Zhang, S.; Wu, Y.; Jin, B.; Shao, M. The Ultrathin Prenucleation Interface-Stabilized Metal Zn Anode Toward high-Performance Flexible Zn-Batteries. *Mater. Today Energy* **2021**, *22*, 100849.
(31) Peng, H.; Liu, C.; Wang, N.; Wang, C.; Wang, D.; Li, Y.; Chen, B.; Yang, J.; Qian, Y. Intercalation of Organics into Layered Structures Enables Superior Interface Compatibility and Fast Charge Diffusion for Dendrite-Free Zn Anodes. *Energy Environ. Sci.* **2022**, *15*, 1682−1693.
(32) Yang, J. L.; Li, J.; Zhao, J. W.; Liu, K.; Yang, P.; Fan, H. J. Stable Zinc Anodes Enabled by a Zincophilic Polyanionic Hydrogel Layer. *Adv. Mater.* **2022**, *34*, 2202382.
(33) Deng, C.; Xie, X.; Han, J.; Tang, Y.; Gao, J.; Liu, C.; Shi, X.; Zhou, J.; Liang, S. A Sieve-Functional and Uniform-Porous Kaolin Layer toward Stable Zinc Metal Anode. *Adv. Funct. Mater.* **2020**, *30*, 2000599.
(34) Liang, P.; Yi, J.; Liu, X.; Wu, K.; Wang, Z.; Cui, J.; Liu, Y.; Wang, Y.; Xia, Y.; Zhang, J. Highly Reversible Zn Anode Enabled by Controllable Formation of Nucleation Sites for Zn-Based Batteries. *Adv. Funct. Mater.* **2020**, *30*, 1908528.
(35) Zhou, S.; Wang, Y.; Lu, H.; Zhang, Y.; Fu, C.; Usman, I.; Liu, Z.; Feng, M.; Fang, G.; Cao, X.; Liang, S.; Pan, A. Anti-Corrosive and Zn-Ion-Regulating Composite Interlayer Enabling Long-Life Zn Metal Anodes. *Adv. Funct. Mater.* **2021**, *31*, 2104361.
(36) Liu, H.; Wang, J. G.; Hua, W.; Sun, H.; Huyan, Y.; Tian, S.; Hou, Z.; Yang, J.; Wei, C.; Kang, F. Building Ohmic Contact Interfaces toward Ultrastable Zn Metal Anodes. *Adv. Sci.* **2021**, *8*, 2102612.
(37) He, X.; Cui, Y.; Qian, Y.; Wu, Y.; Ling, H.; Zhang, H.; Kong, X. Y.; Zhao, Y.; Xue, M.; Jiang, L.; Wen, L. Anion Concentration Gradient-Assisted Construction of a Solid-Electrolyte Interphase for a Stable Zinc Metal Anode at High Rates. *J. Am. Chem. Soc.* **2022**, *144*, 11168−11177.
(38) Gao, Y.; Cao, Q.; Pu, J.; Zhao, X.; Fu, G.; Chen, J.; Wang, Y.; Guan, C. Stable Zn Anodes with Triple Gradients. *Adv. Mater.* **2023**, *35*, 2207573.
(39) Cao, Q.; Gao, Y.; Pu, J.; Zhao, X.; Wang, Y.; Chen, J.; Guan, C. Gradient Design of Imprinted Anode for Stable Zn-Ion Batteries. *Nat. Commun.* **2023**, *14*, 641.
(40) Schroeder, U.; Park, M. H.; Mikolajick, T.; Hwang, C. S. The Fundamentals and Applications of Ferroelectric HfO_2. *Nat. Rev. Mater.* **2022**, *7*, 653−669.
(41) Zhao, Z.; Zhao, J.; Hu, Z.; Li, J.; Li, J.; Zhang, Y.; Wang, C.; Cui, G. Long-Life and Deeply Rechargeable Aqueous Zn Anodes Enabled by a Multifunctional Brightener-Inspired Interphase. *Energy Environ. Sci.* **2019**, *12*, 1938−1949.
(42) Harishsenthil, P.; Chandrasekaran, J.; Marnadu, R.; Balasubramani, V. Incorporation of Zn Ions on High Dielectric HfO2 Thin Films by Spray Pyrolysis and Fabrication of Al/Zn@HfO2/n-Si Schottky Barrier Diodes. *Sens. Actuators, A* **2021**, *331*, 112725.
(43) Chu, Y.; Zhang, S.; Wu, S.; Hu, Z.; Cui, G.; Luo, J. In Situ Built Interphase with High Interface Energy and Fast Kinetics for High Performance Zn Metal Anodes. *Energy Environ. Sci.* **2021**, *14*, 3609−3620.

(44) Liu, Q.; Wang, Y.; Hong, X.; Zhou, R.; Hou, Z.; Zhang, B. Elastomer-Alginate Interface for High-Power and High-Energy Zn Metal Anodes. *Adv. Energy Mater.* **2022**, *12*, 2200318.
(45) Zhou, M.; Guo, S.; Li, J.; Luo, X.; Liu, Z.; Zhang, T.; Cao, X.; Long, M.; Lu, B.; Pan, A.; Fang, G.; Zhou, J.; Liang, S. Surface-Preferred Crystal Plane for a Stable and Reversible Zinc Anode. *Adv. Mater.* **2021**, *33*, 2100187.
(46) Chen, A.; Zhao, C.; Guo, Z.; Lu, X.; Liu, N.; Zhang, Y.; Fan, L.; Zhang, N. Fast-Growing Multifunctional $ZnMoO_4$ Protection Layer Enable Dendrite-Free And Hydrogen-Suppressed Zn Anode. *Energy Storage Mater.* **2022**, *44*, 353−359.
(47) Zheng, J.; Zhu, G.; Liu, X.; Xie, H.; Lin, Y.; Zeng, Y.; Zhang, Y.; Gandi, A. N.; Qi, Z.; Wang, Z.; Liang, H. Simultaneous Dangling Bond and Zincophilic Site Engineering of SiN_x Protective Coatings toward Stable Zinc Anodes. *ACS Energy Lett.* **2022**, *7*, 4443−4450.
(48) Chen, S.; Chen, J.; Liao, X.; Li, Y.; Wang, W.; Huang, R.; Zhao, T.; Yan, S.; Yan, Z.; Cheng, F.; Wang, H. Enabling Low-Temperature and High-Rate Zn Metal Batteries by Activating Zn Nucleation with Single-Atomic Sites. *ACS Energy Lett.* **2022**, *7*, 4028−4035.
(49) Chen, T.; Huang, F.; Wang, Y.; Yang, Y.; Tian, H.; Xue, J. M. Unveiling the Synergistic Effect of Ferroelectric Polarization and Domain Configuration for Reversible Zinc Metal Anodes. *Adv. Sci.* **2022**, *9*, 2105980.
(50) Bie, Z.; Yang, Q.; Cai, X.; Chen, Z.; Jiao, Z.; Zhu, J.; Li, Z.; Liu, J.; Song, W.; Zhi, C. One-Step Construction of a Polyporous and Zincophilic Interface for Stable Zinc Metal Anodes. *Adv. Energy Mater.* **2022**, *12*, 2202683.
(51) Wang, T.; Wang, P.; Pan, L.; He, Z.; Dai, L.; Wang, L.; Liu, S.; Jun, S. C.; Lu, B.; Liang, S.; Zhou, J. Stabling Zinc Metal Anode with Polydopamine Regulation through Dual Effects of Fast Desolvation and Ion Confinement. *Adv. Energy Mater.* **2023**, *13*, 2203523.
(52) Cao, Q.; Pan, Z.; Gao, Y.; Pu, J.; Fu, G.; Cheng, G.; Guan, C. Stable Imprinted Zincophilic Zn Anodes with High Capacity. *Adv. Funct. Mater.* **2022**, *32*, 2205771.
(53) Liang, G.; Zhu, J.; Yan, B.; Li, Q.; Chen, A.; Chen, Z.; Wang, X.; Xiong, B.; Fan, J.; Xu, J.; Zhi, C. Gradient Fluorinated Alloy to Enable Highly Reversible Zn-Metal Anode Chemistry. *Energy Environ. Sci.* **2022**, *15*, 1086−1096.
(54) Guo, J.; Ming, J.; Lei, Y.; Zhang, W.; Xia, C.; Cui, Y.; Alshareef, H. N. Artificial Solid Electrolyte Interphase for Suppressing Surface Reactions and Cathode Dissolution in Aqueous Zinc Ion Batteries. *ACS Energy Lett.* **2019**, *4*, 2776−2781.
(55) Wan, F.; Zhang, L.; Dai, X.; Wang, X.; Niu, Z.; Chen, J. Aqueous Rechargeable Zinc/Sodium Vanadate Batteries with Enhanced Performance from Simultaneous Insertion of Dual Carriers. *Nat. Commun.* **2018**, *9*, 1656.
(56) Hu, P.; Zhu, T.; Wang, X.; Wei, X.; Yan, M.; Li, J.; Luo, W.; Yang, W.; Zhang, W.; Zhou, L.; Zhou, Z.; Mai, L. Highly Durable $Na_2V_6O_{16}\cdot 1.63H_2O$ Nanowire Cathode for Aqueous Zinc-Ion Battery. *Nano Lett.* **2018**, *18*, 1758−1763.
(57) Li, S.; Liu, Y.; Zhao, X.; Shen, Q.; Zhao, W.; Tan, Q.; Zhang, N.; Li, P.; Jiao, L.; Qu, X. Sandwich-Like Heterostructures of MoS_2/Graphene with Enlarged Interlayer Spacing and Enhanced Hydrophilicity as High-Performance Cathodes for Aqueous Zinc-Ion Batteries. *Adv. Mater.* **2021**, *33*, 2007480.
(58) Qin, Y.; Li, H.; Han, C.; Mo, F.; Wang, X. Chemical Welding of the Electrode-Electrolyte Interface by Zn-Metal-Initiated In Situ Gelation for Ultralong-Life Zn-Ion Batteries. *Adv. Mater.* **2022**, *34*, 2207118.

https://doi.org/10.1021/acsenergylett.3c00367
ACS Energy Lett. 2023, 8, 2042−2050